Ocean Dynamics (2007) 57:559–578
DOI 10.1007/s10236-007-0126-1

Barotropic and baroclinic processes in the transport variability of the Antarctic Circumpolar Current

Dirk Olbers · Karsten Lettmann

Received: 3 May 2007 / Accepted: 21 August 2007 / Published online: 24 October 2007

Abstract Synoptic scale variability of the Southern Ocean wind field in the high-frequency range of barotropic Rossby waves results in transport variations of the Antarctic Circumpolar Current (ACC), which are highly coherent with the bottom pressure field all around the Antarctic continent. The coherence pattern, in contrast to the steady state ACC, is steered by the geostrophic f/h contours passing through Drake Passage and circling closely around the continent. At lower frequencies, with interannual and decadal periods, the correlation with the bottom pressure continues, but baroclinic processes gain importance. For periods exceeding a few years, variations of the ACC transport are in geostrophic balance with the pressure field associated with the baroclinic potential energy stored in the stratification, whereas bottom pressure plays a minor role. The low-frequency variability of the ACC transport is correlated with the baroclinic state variable in the entire Southern Ocean, mediated by baroclinic topographic–planetary Rossby waves that are not bound to f/h contours. To clarify the processes of wave dynamics and pattern correlation, we apply a circulation model with simplified physics (the barotropic–baroclinic-interaction model BARBI) and use two types of wind forcing: the National Centers for Environmental Prediction (NCEP) wind field with integrations spanning three decades and an artificial wind field constructed from the first three empirical orthogonal functions of NCEP combined with a temporal variability according to an autoregressive process. Experiments with this Southern Annular Mode type forcing have been performed for 1,800 years. We analyze the spin-up, trends, and variability of the model runs. Particular emphasis is placed on coherence and correlation patterns between the ACC transport, the wind forcing, the bottom pressure field and the pressure associated with the baroclinic potential energy. A stochastic dynamical model is developed that describes the dominant barotropic and baroclinic processes and represents the spectral properties for a wide range of frequencies, from monthly periods to hundreds of years.

Keywords Antarctic circumpolar current · ACC transport · Coherence patterns

1 Introduction

The transport of the Antarctic Circumpolar Current (ACC) shows a strong dependence on the strength of the windstress over the Southern Ocean. A unified relation, however, could not be found and may in fact not exist in a simple but general form because many processes inherent in the fluid dynamics of the circumpolar ocean—topographic and eddy-induced stresses as well as effects of stratification—interact with the forcing and compete to shape the circulation (see e.g., the recent reviews by Rintoul et al. 2001; Olbers et al. 2004). With respect to variations of the ACC transport, a simpler picture is sketched by various recent studies set afoot by the work of Hughes et al. (1999) on what they called 'the Southern Mode' of variability. The ACC transport was found to be highly correlated with the bottom pressure all around the Antarctic

Responsible editor: Richard Greatbatch

D. Olbers (✉) · K. Lettmann
Alfred Wegener Institute for Polar and Marine Research, Bremerhaven, Germany
e-mail: dirk.olbers@awi.de

coast and with the winds over the circumpolar area. Early investigations of this issue date back to Wearn and Baker (1980) and Whitworth and Peterson (1985). Hughes et al. (1999) offer an explanation of the large-scale coherent response on the basis of the propagation characteristics of topographically modified barotropic Rossby waves described by the barotropic vorticity balance. These waves, excited resonantly by the varying wind, mediate the response along the geostrophic contours $f/h = \text{const}$ that pass in a narrow tunnel through the southern part of Drake Passage and encircle the continent.

Southern Ocean winds are varying over a broad range of temporal scales, and correlations were discovered from inertial to synoptic and decadal periods; the latter periods and associated coherence pattern are summarized as the Southern Annual Mode (SAM, Thompson and Wallace 2000). To mention a few recent important studies: Meredith et al. (1996) and Hughes et al. (1999) investigate correlation of the ACC transport with winds and bottom pressure records; satellite altimetry is used by Gille (1999) and Vivier et al. (2005); and coastal tide gauges by Aoki (2002). Some correlation studies have addressed also the output from numerical models, partly in combination with real data (e.g., Hughes et al. 2003; Meredith et al. 2004; Weijer and Gille 2005; Hughes and Meredith 2006).

The correlation between transport and bottom pressure should continue to periods longer than decadal, culminating in the geostrophic relation in steady state. At some instance, however, baroclinic pressure variations and baroclinic Rossby waves must come into play because, with increasing timescales, a growing part of the transport is found in the shear component of the current and, speaking in dynamical terms, the baroclinic pressure torque overwhelms the windstress curl in the integrated vorticity balance, and the pressure described by the baroclinic potential energy dominates the bottom pressure in terms of geostrophy (see e.g., Olbers et al. 2006). The transition of the so far high-frequency Southern Mode to this low-frequency response and the associated dynamical regime is the topic of the present study. The switch from a barotropic response in the fluctuations to a baroclinic one should occur when baroclinic Rossby waves can be resonantly excited. Willebrand et al. (1980) suggest that this transition occurs at the shortest period of the baroclinic mode.

We analyze the large-scale coherent pattern between transport, windstress, and pressure variables in simulations with a simplified circulation model driven by windstress over decades to many centuries. The wind field is either observed (a few decades of the National Centers for Environmental Prediction [NCEP] reanalysis) or artificial (an autoregressive [AR] SAM type wind). The model is the two-mode version of barotropic–baroclinic interaction (BARBI ocean model, Olbers and Eden 2003), which in its essence is a coupled barotropic–baroclinic wave model with forcing, advection, and parameterized eddy processes incorporated. The model contains baroclinic gravity waves and barotropic and baroclinic Rossby waves, modified and coupled by the topography that BARBI can represent in a realistic way. Topography and stratification determine the propagation characteristics and dispersion of the wave modes that can be excited by variable wind forcing. Gravity waves are mainly responsible for the local geostrophic adjustment, and Kelvin waves spread signals along the Antarctic and South American coast in a narrow strip of the size of the baroclinic Rossby radius. With the rigid-lid approximation used in most models (also in our model), the barotropic gravity waves are infinitely fast, and the signal propagation by gravity waves is entirely in the baroclinic mode, but Rossby waves have both components, a high-frequency barotropic and a low-frequency baroclinic mode. They propagate signals across the ocean interior.

Both Rossby modes are influenced by topography but barotropic waves have much stronger steering by topographic features, mathematically imprinted in the f/h contours, than baroclinic ones. The low-frequency response (decadal to centuries) is thus governed to an increasing degree by baroclinic dynamics with variables which have correlation patterns that are independent of the f/h tunnel through Drake Passage. In the range of ultra-long periods, well above a decade, variations of the ACC transport have most of their power in variations of the shear current with the baroclinic potential energy as associated geostrophic pressure field. The paper investigates dynamics of the high- and low-frequency regimes with a coherence and correlation analysis, regression models and stochastic-dynamical models.

The paper is organized as follows. Section 2 gives an introduction of the processes and timescales that govern steady and fluctuating states of the ACC. The model setup and the different wind forcing fields are explained in Section 3, and the spin-up is analyzed in Section 4, including some linear model concepts. A comparison of the transport variability, obtained from the BARBI simulations, with observation of the ACC transport from hydrography and from numerical eddy-resolving models is found in Section 5, and finally, in the Sections 6 and 7, we discuss the coherence and correlation pattern between the ACC transport, pressure gradients, and windstress of the simulations, supporting the interpretation by simple linear regression

and stochastic models. The last section is a concluding discussion of our findings. We have added two appendices. In Appendix 1, we give a short summary of the BARBI model. In Appendix 2, we derive the flat-bottom and topographic wave properties of the model.

2 Processes and timescales in steady and fluctuating states of the ACC

The circulation model used in this study is a two-mode version of the BARBI model (Olbers and Eden 2003). The physics of the BARBI model—the governing equations and parameterizations—are briefly outlined in Appendix 1. The fundamental variables describing the flow in BARBI are the vertically integrated velocity $\mathbf{U} = \int \mathbf{u} dz = (-\partial\psi/\partial y, \partial\psi/\partial x)$ or its streamfunction ψ, and the baroclinic potential energy $E = g\int z\rho dz$ stored in the density perturbation ρ about a mean profile with Brunt–Väisälä frequency N. Both these variables are vertically integrated from top to the ocean depth at $z = -h$, and $\mathbf{U}$ or ψ reflect fast barotropic timescales, whereas E is a baroclinic variable with slow baroclinic timescales. Whereas $\mathbf{U}$ and E are prognostic variables, the other important variable in the BARBI model, the bottom pressure P (barotropic plus baroclinic), is calculated diagnostically (see Appendix 1).

The low-frequency version of BARBI's governing equations 12 to 15 is the coupled set of the barotropic vorticity balance and the balance of baroclinic potential energy that may be cast into the form[1]

$$\frac{\partial}{\partial t}\nabla\cdot\frac{1}{h}\nabla\psi + \mathcal{J}\left(\psi,\frac{f}{h}\right) = \mathcal{J}\left(E,\frac{1}{h}\right) + \mathrm{curl}\,\frac{\boldsymbol{\tau}}{h} + A\blacktriangledown^4\psi \quad (1)$$

$$\frac{\partial E}{\partial t} + h\mathbf{U}\cdot\nabla\frac{E}{h^2} + \mathcal{J}(E, f\lambda^2) - \mathcal{J}(\psi, f^2\lambda^2) = -\mathrm{curl}\, f\lambda^2\boldsymbol{\tau} + \mathcal{Q} - \mathcal{D} + K\nabla^2 E \quad (2)$$

where $\lambda = Nh/(\sqrt{6}|f|)$ is the local internal Rossby radius in the BARBI frame. The first equation is derived by taking the curl of the balance of the depth-averaged velocity $\mathbf{U}/h$, and the second is derived in this form from the BARBI model equations 13 and 15 by taking the baroclinic velocity moment balance (13) diagnostically, which filters out baroclinic gravity waves and short baroclinic Rossby waves. In Eq. 1, we notice the advection of planetary–topographic vorticity and the JEBAR torque associated with density and topography gradients, both written as Jacobians, and the forcing, friction, and the tendency terms. Equation 2 reflects the balance of vertical pumping by geostrophic, barotropic, and Ekman velocities (the third and fourth terms on the left hand side and the first term on the right hand side, respectively), acting on the mean stratification, given by N, in the generation of potential energy. In the following discussion, these equations serve to discuss the processes and timescales of the steady ACC circulation and its variability. We draw from Olbers et al. (2006) who have analyzed the steady circulation of the ACC and its dynamical balance, modeled with BARBI, and from Hughes et al. (1999) who have introduced and described the concept of 'a Southern Mode' of variability in the Southern Ocean. Vivier et al. (2005) have substantiated this concept by extensive data analysis and numerical experimentation with a barotropic model.

In the context of studying variability with the BARBI model, it seems appropriate to mention the wave properties of the two-mode version. A linear wave analysis based on Eqs. 1 and 2 (see Appendix 2) shows that the low-frequency version of BARBI has the familiar set of mixed barotropic–baroclinic Rossby waves of topographic–planetary dynamics (see e.g., Rhines 1977). The two-mode BARBI model may thus be interpreted as the coupled mixed planetary–topographic wave problem for the first two modes, with forcing by windstress as well as friction, diffusion, and advective nonlinearities included. The modes are neither strictly barotropic nor strictly baroclinic if topographic slopes are present. They are of a mixed quality (details are found in Appendix 2) and very similar to the two-layer quasigeostrophic modes analyzed by Hallberg (1997). Note that topography is implemented in BARBI without any depth scaling as, e.g., required in quasi-geostrophic models.

The steady state Provided that topography is present, the circulation in a homogeneous ocean differs substantially from the case of a stratified ocean. In the first case, $E \equiv 0$, there is no JEBAR, and only the advection of f/h-vorticity, wind forcing, and friction remain in the vorticity balance (1). The latter two terms determine the flow across f/h contours. The balance, however, allows for 'free' flow along the contours, $\psi = fct(f/h)$, which of course is not entirely free because it is affected and coupled to the forced part of the solution by friction. As the f/h contours are largely expelled from Drake Passage, the current through the passage is of minor size. A large bottom formstress is opposing the wind in the zonally mean balance of momentum. The circumpolar flow in this barotropic setting is thus along a bundle of f/h contours that close around Antarctica

[1] The nabla-4 operator $\blacktriangledown^4$ is similar to the familiar ∇^4 but modified by the depth h, see Olbers et al. (2006).

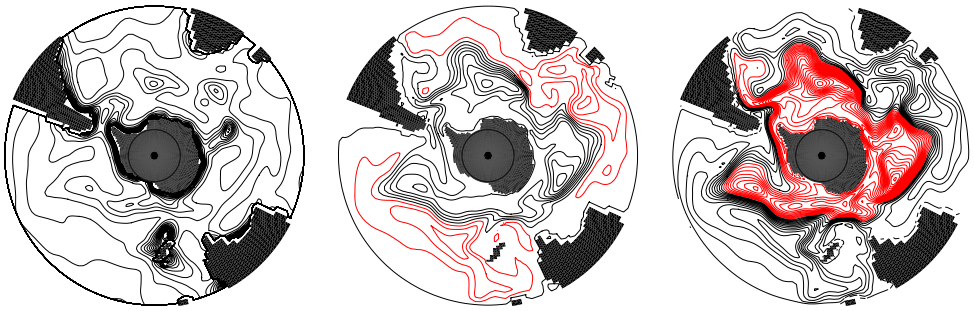

Fig. 1 *Left* geostrophic contours f/h, CI = 5×10^{-9} m^{-1} s^{-1}. *Middle and right* steady solution obtained with the barotropic BARBI model forced by NCEP windstress. *Middle* streamfunction, CI = 10 Sv. *Right* bottom pressure, CI = 0.1 m^2 s^{-2}. Positive contours are *black, negative red*

in a narrow strip along the continental slope. There are, however, large-scale circulation cells with quite substantial currents in areas with closed f/h contours, occurring over the mid-ocean ridge in the South Atlantic and Indian Ocean and around Kerguelen Plateau. The circulation is exemplified in Fig. 1 with the steady BARBI solution (forcing and model setup are given below). It clearly is a quite unrealistic simulation of the ACC.

When the system has approached equilibrium in a stratified case with topography, the Jacobian terms in each of the above balances (1) and (2) overwhelm the remaining terms. As shown in Olbers et al. (2006), they can be related to vertical velocities induced by either the barotropic flow (the ψ-terms) or by the geostrophic baroclinic flow (the E-terms) induced by crossing of the topography by the current. The potential energy is found to be almost constant along the flow. A reasonable approximation is $E \sim f\psi + \text{const}$, and the potential energy balance may be used in a rigorous expansion to express the Jacobians in the vorticity balance in a new form with the result

$$\frac{3}{2}\beta\frac{\partial\psi}{\partial x} - Ah\blacktriangledown^4\psi + \frac{K}{\lambda^2}\nabla^2\psi = h\,\mathrm{curl}\,\frac{\boldsymbol{\tau}}{h} + \frac{1}{2}\frac{f}{h^2}\,\mathrm{curl}\,\frac{h^2\boldsymbol{\tau}}{f} - \frac{1}{2}\frac{\mathcal{Q}-\mathcal{D}}{f\lambda^2} \tag{3}$$

We should emphasize that this balance becomes valid only after the spin-up to steady state because it is based upon the balance of the Jacobians. It is evident that the baroclinic JEBAR forcing overcomes the constraint of the f/h term and restores zonal characteristics. It also introduces a modified forcing by wind and buoyancy flux $\mathcal{Q}$ and dissipation $\mathcal{D}$. Olbers et al. (2006) call Eq. 3 the 'baroclinic Stommel equation' because the viscosity term is outweighed by far by the eddy diffusivity term taking the place of Stommel's bottom friction (note that Kf^2/N^2 is an effective vertical diffusivity of momentum). The stratified ACC solution is exemplified in Fig. 2, again obtained with the BARBI model. Evidently, f/h contours do not shape the current any more. According to Eq. 3, 'free' flow is now possible along latitude circles through Drake Passage, but the bottom formstress is as efficient as before to balance to a large degree the zonal forcing of the mean current. Note, however, that the bottom pressure has still imprints of the f/h contours and resembles to some degree the pressure of the homogeneous system (compare the right most panels of Fig. 1 and Fig. 2). The reason for this behavior is that the f/h contours are still dominating the pressure in the Poisson equation 18. A very approximate solution of the latter is $P \sim (f/h)\,(\psi - E/f)$. The bottom pressure gradient is small compared to the pressure gradient induced by the potential energy. The current $\mathbf{U}$ is thus in approximate geostrophic balance with ∇E.

The fluctuating state The balance conditions in Eqs. 1 and 2 change completely when transient behavior occurs. Trivially, the tendency terms are gaining importance, but we must realize the totally different sizes of the natural timescales in these equations. The natural timescale of the streamfunction ψ (or integrated ve-

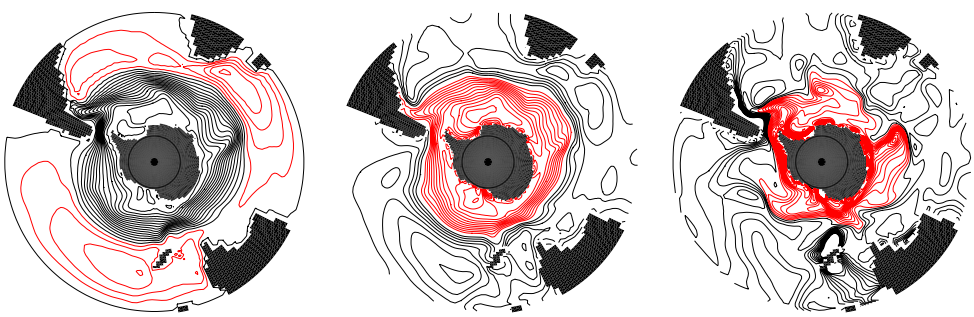

Fig. 2 Steady solution obtained with the BARBI model LN forced by NCEP windstress. *Left* streamfunction, CI = 10 Sv. *Middle* baroclinic potential energy, CI = 1,000 m^3 s^{-2}. *Right* bottom pressure, units: CI = 0.1 m^2 s^{-2}

locity) is found from Eq. 1 to be of order $1/(\beta_{\text{eff}} L)$, whereas the baroclinic equation 2 reveals $L/(\beta_{\text{eff}} \lambda^2)$ for the timescale of variations of the potential energy E. In this study, β_{eff} includes the topographic β, and L is a lateral length scale. The timescale of ψ relates to the period of barotropic Rossby waves and the timescale of E to the period of baroclinic Rossby waves. The periods of these modes differ by the very large ratio L^2/λ^2. Their group velocities are highly different as well: Barotropic Rossby waves, with a speed of a few meters per second, can travel once around Antarctica in a few months, and baroclinic waves need a much longer time, a few years. The speed of the baroclinic mode, a few centimeters per second in the flat-bottom case, is generally slower than that of the mean flow so that its natural westward propagation is reverted by the strong eastward ACC: Baroclinic waves in the ACC are supercritical.

The fast response of the coupled barotropic-baroclinic system on timescales up to a few months is evidently governed by barotropic dynamics. Fluctuations in the wind-forcing excite barotropic planetary–topographic Rossby waves which are balanced by the two terms on the left hand side of Eq. 1. The baroclinic potential energy is only slowly responding and the JEBAR term can be taken constant at a first approximation. It drives the mean flow as outlined above. In a more refined approximation, variations of E can be described within the framework of the stochastic climate model of Hasselmann (1976): the slow baroclinic subsystem—the potential energy (and JEBAR)—integrate the fast 'stochastic' forcing implemented by the windstress (the Ekman pumping term in Eq. 2) and the barotropic pumping acting of the mean stratification (the ψ-Jacobian in Eq. 2). In contrast to the classical stochastic model this forcing is a red-noise.

The geostrophic contours regain importance in the fluctuating state because long barotropic waves propagate along constant f/h. For the waves in BARBI we demonstrate this by a Wentzel–Kramer–Brillouin

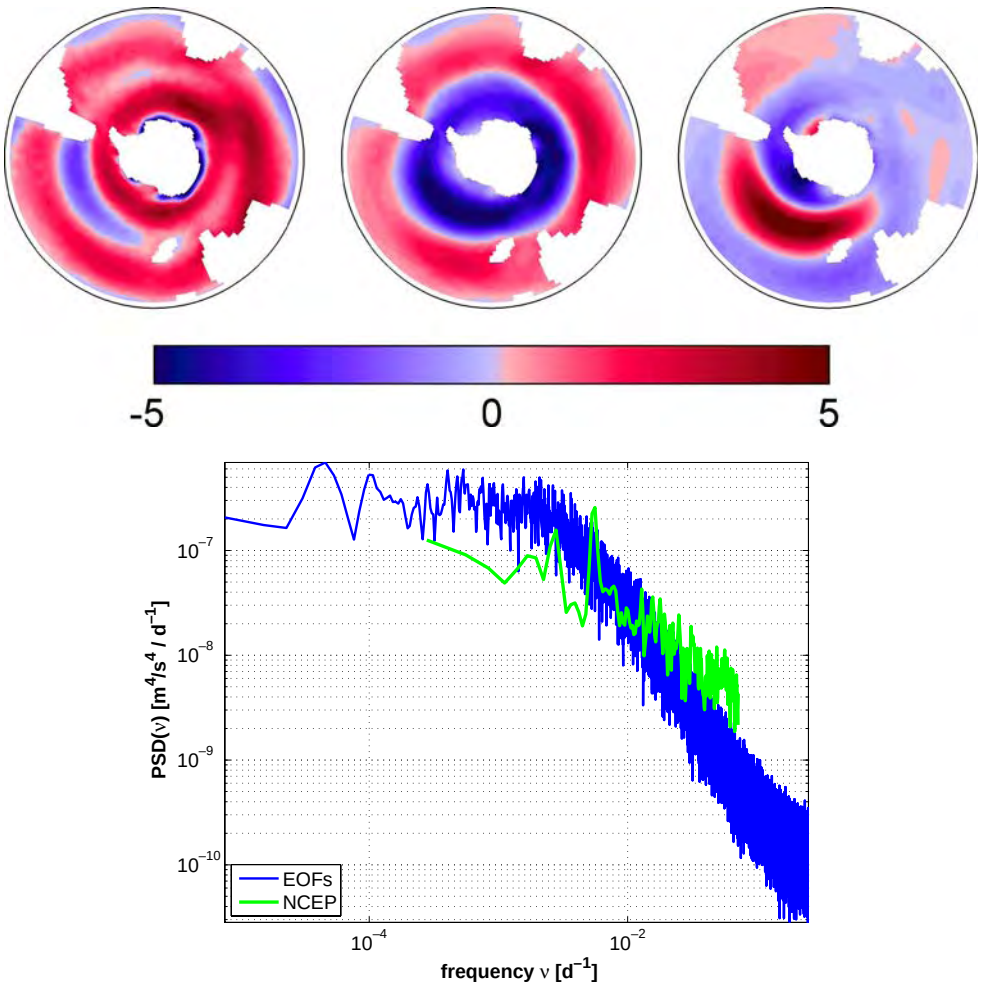

Fig. 3 *Upper row* the first three EOFs of the NCEP zonal windstress, units 10^{-5} m^{2}s^{-2}. *Lower row* power spectral density of the zonal windstress for NCEP (*green*) and AR (*blue*)

(WKB) analysis which, however, might be questioned in view of the large wavelengths involved: 'long' should be compared to the external Rossby radius $\sqrt{gh/f} \sim$ 2,000 km. This value is as well roughly the size of the coherence scale of synoptic wind fluctuations (see Fig. 3). Nevertheless, the fast response to wind driving in the Southern Ocean seems to be mediated along these contours and thus is mainly visible in the tunnel of f/h contours that pass around Antarctica close to the continental slope. This feature strongly distinguishes the fluctuating response from that of the steady state (in the presence of stratification), and as stated by Hughes et al. (1999), 'it makes little sense to think of wind-driven fluctuations as changes in the strength of the mean flow'. As the transients are barotropic, the associated currents are in balance with the bottom pressure gradients, not like the mean flow, which is mainly coupled to spatial variations of the potential energy. In this fluctuating state, the bottom pressure is thus highly coherent in the area around Antarctica bounded by the northernmost closed f/h contour. The pressure fluctuations in this 'tunnel area' is negatively correlated with transport fluctuation of the ACC due to the constraint of geostrophy. Hughes et al. (1999) refer to this regime of wind-driven transport fluctuations as 'the Southern Mode'. Variations of the ACC transport on these fast timescales can thus be monitored by the variations of bottom pressure in the southern Drake Passage or at other locations around the Antarctic continent. It has been documented in many studies, applying a correlation to bottom pressure records (e.g., Meredith et al. 1996; Hughes et al. 1999), satellite altimetry (e.g., Gille 1999; Vivier et al. 2005), coastal tide gauges (e.g., Aoki 2002), and wind data, part of them also in combination with output from numerical models. The Southern Mode is the ocean response to the SAM (Thompson and Wallace 2000) on synoptic timescales. This connection was explicitly drawn by Hughes et al. (2003).

A similar response in the bottom pressure and correlation with the ACC transport is also taking place on interannual and longer timescales, as suggested by Hall and Visbeck (2002) and found by Meredith et al. (2004) in bottom pressure records and output from the Ocean Circulation and Climate Advanced Modelling (OCCAM) 1/4° model. As an extension of the barotropic Southern Mode we expect a corresponding large-scale coherence pattern with the potential energy field for slower baroclinic timescales, i.e., above a few years. Baroclinic Rossby waves are not bound to the f/h contours and hence, the coherence of transport and E should not be constrained by these contours. This conjecture is the issue of the present investigation. Some of the results reported in the following derive from the thesis of Lettmann (2006).

3 Model set-up and forcing functions

The present applications of BARBI uses a model domain from 76 to 20°S with a resolution of $2° \times 1°$. Topography data from the ETOPO5 data set are interpolated onto the model grid. The geostrophic contours $f/h =$ const of the model are displayed in Fig. 1. The Drake Passage of the model is open between 62.5 and 55.5°S. Note that only a small bundle of f/h contours passes through very close to the Antarctic continent. The parameters of the simulations presented in this study are slightly different from those in Olbers et al. (2006). The horizontal viscosity is $A = 5 \times 10^4$ m^2 s^{-1}, and the eddy diffusivity is $K = 2 \times 10^3$ m^2 s^{-1}. We use a linear damping form $\mathcal{D} = \mu E$ for the dissipation of potential energy with a coefficient $\mu = 1.5 \times 10^{-10}$ s^{-1}. Two versions of the full baroclinic model are used, differing in the Brunt–Väisälä frequency: Model SN has $N = 1.5 \times 10^{-3}$ s^{-1}, whereas model LN has a slightly larger $N = 1.8 \times 10^{-3}$ s^{-1}. The corresponding baroclinic Rossby radii are $\lambda_{SN} = 19.3$ km and $\lambda_{LN} = 23.3$ km, respectively. The barotropic version is obtained by taking $N \equiv 0$.

BARBI can be forced by a surface windstress and by a source of the baroclinic potential energy (the $\mathcal{Q}$ term in Eqs. 15 and 2). The latter is set to zero in the present experiments, and thus, a purely wind-driven variability of the Southern Ocean circulation is studied. Two different kinds of wind forcing are used: The first one (NCEP wind) are daily winds from NCEP/National Center for Atmospheric Research (NCAR) for the time span 1948 to 2006, and the second type (AR wind) is an artificial windstress derived from the first three empirical orthogonal functions (EOFs) of the NCEP/NCAR monthly winds and the long-term mean windstress $\bar{\boldsymbol{\tau}}(x, y)$ vector field from 1948 to 2006. The AR windstress for the zonal components has the form

$$\tau^x(x, y, t) = \bar{\tau}^x(x, y) + \sum_{i=1}^{3} a_i(t) \cdot \sigma_i^2 \cdot EOF_i^x(x, y) \qquad (4)$$

Table 1 Variances of the first three EOF of the NCEP windstress vector

	EOF_1	EOF_2	EOF_3
Zonal	0.263	0.144	0.071
Meridional	0.355	0.065	0.056

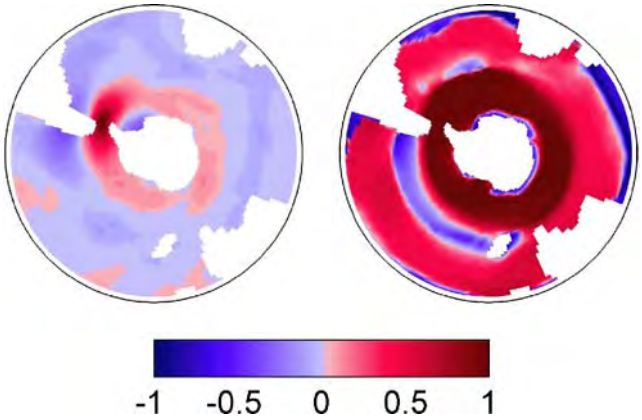

Fig. 4 Correlation of the zonal windstress in Drake Passage with the zonal windstress in the Southern Ocean (*left* NCEP, *right* AR)

where σ_i is the variance by the i-th EOF of τ^x. It controls the influence of the different EOFs to the windstress. The EOFs of the zonal windstress are displayed in Fig. 3 (they are renormalized to carry the units of windstress according to von Storch and Zwiers (1999)). The meridional component is modeled in a similar way; the σ_i, however, are different for the two vector components (see Table 1), and also, the amplitudes $a_i(t)$are different. They are red noise time series with mean zero of the AR-form

$$a_i(t) = \alpha a_i(t - \Delta t) + Z(t) \tag{5}$$

with $\alpha = 0.98$ and white noise $Z(t)$, which are equally distributed random numbers on the interval $[-3.0, 3.0]$ (for the vector windstress, six independent realizations are generated). A comparison of the spectral density of the NCEP windstress with the AR-stress for τ^x is given in Fig. 3. The spectra of NCEP and the AR-stress are dissimilar. For periods exceeding a year, the AR-stress is white, and for higher frequencies, we find the well-known ν^{-2} power law of a first-order AR process. The NCEP data cover only a fairly limited range of frequencies, emerging into a ν^{-1} frequency dependence in the high-frequency range. Note that the annual and semi-annual peaks are visible. Also the spatial coherence in NCEP and AR is drastically different. By construction from only a few EOFs, the AR wind has extracted the large-scale coherent pattern of the SAM. As demonstrated in the lower middle and right panels of Fig. 4, the NCEP stress has a zonal correlation scale of roughly 2,000 km. In contrast, the AR stress is highly coherent all around Antarctica according to the SAM pattern.

4 Analysis of spin-up

All experiments are started from a state of rest, forced with the time mean windstress $\bar{\boldsymbol{\tau}}(x, y)$, and integrated to equilibrium, which then is used as initial state for the experiments with variable winds. Various steady circulations with barotropic and baroclinic conditions are discussed in Olbers et al. (2006). The barotropic model has an ACC transport of 29.5 Sv with streamfunction, and the bottom pressure predominantly follows f/h contours (see Fig. 1). The baroclinic simulations get reasonably sized circumpolar flow with little apparent influence of the underlying topography in the streamfunction. The baroclinicity overrides the effect of the f/h contours, as described in Section 2. Figure 2 exemplifies the solutions by depicting the streamfunction, the potential energy, and the bottom pressure for NCEP forcing and model version LN. The steady ACC transport T_0 in this simulation is 141 Sv. Model version SN with a smaller N yields 110 Sv, which is in accordance with the scaling $T_0 \sim \tau^x/(Kf^2/N^2)$ derived in Olbers et al. (2006). The linear relation between transport and the windstress is due to setting K to a constant. More elaborate parameterizations of K would result in other power laws, all of which are questionable as discussed in various studies with numerical models (see, e.g., Tansley and Marshall 2001; Gent et al. 2001; and the review by Olbers et al. 2004). Note that the potential energy follows the streamlines quite closely, whereas the bottom pressure has a tendency to follow the f/h contours and therefore has some resemblance to the barotropic flow. In the geostrophic balance of the vertically integrated velocity, the influence of the bottom pressure is overwhelmed by the pressure associated with the potential energy field that is fairly zonal as the current. The streamfunction shows a distinct Weddell Sea gyre and a weak Ross Sea gyre.

The approach of the circulation toward the steady solution is more or less of exponential form. For the total transport through Drake Passage, we find $T(t) = T_0(1 - e^{-t/t_T})$ as displayed in Fig. 5 and suggested by the simple relaxation model of Wearn and Baker (1980),

$$\dot{T} + \frac{T}{t_T} = B\tau^x \tag{6}$$

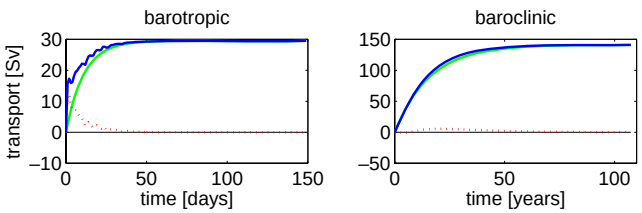

Fig. 5 ACC transport during spin-up from a state of rest after switching on the windstress. *Left* barotropic regime with $N = 0$ (the sampling time step is 3 days). *Right* baroclinic regime with $N = 0.0018\ \mathrm{s}^{-1}$ (model LN, the sampling time step is 800 days). *Blue* actual transport, *green* exponential fit from Eq. 6, *red* difference

where $\tau^x(t)$ is a measure of the zonally averaged zonal windstress (with time mean τ_0) and B the width of the current. Wearn and Baker estimate the relaxation time t_T from the steady solution $T_0 = t_T B\tau_0$, and using reasonable values for T_0, B and τ_0, they find a surprisingly small value of $t_T = 7$ days.

Assuming that Eq. 6 is valid as well as for fluctuating state, we interpret $T(t)$ as a random excursion about a mean transport, which is driven by the noise in the forcing $\tau^x(t)$. Equation 6 then becomes a stochastic differential equation (it is an Ornstein–Uhlenbeck process). The system is an example of Hasselmann's (1976) stochastic climate model. We will proceed along this approach in Section 7. Wearn and Baker apply a lagged correlation analysis of time series of the observed circumpolar averaged windstress and the transport evaluated from the observed pressure difference across Drake Passage and find a lead of the wind by about 8 to 9 days, close to damping timescale of the spin-up model. The authors refer to the very fast long gravity waves to mediate such a fast response. Gravity waves, however, are important in the geostrophic adjustment, taking place on a rather regional scale. In BARBI, as in other rigid-lid models, these fast gravity waves are filtered out. In view of the f/h modulated correlation behavior found later by other studies (see Section 2 and below), it is more likely that barotropic Rossby wave propagation works in the short relaxation on the very large scales. These waves can travel around Antarctica within a few days to a month (see Table 2 for the timescales of different processes).

The spin-up of the barotropic BARBI simulation follows quite closely the Wearn–Baker model with a timescale of $t_{\text{trop}} = 11$ days for our particular forcing and model configuration. As shown in Fig. 5 (left panel), there are fluctuations of transport in the first few days, which likely are associated with barotropic planetary–topographic Rossby waves. They help adjust the transport to its steady state value that is then governed by friction, topography height, and the geometry of the f/h contours. In Table 2, we give estimates of frictional, diffusive, advective, and wave propagation times. For the circulation through the narrow f/h tunnel in the barotropic case, frictional and wave timescales are indeed of the order of t_{trop}. Further details on these wave equilibration processes are given by Olbers et al. (2006), and for a low-order version of the relevant balances, see Olbers et al. (2007). To determine the barotropic time constant, the barotropic Rossby waves in the transport record were smoothed with a Gaussian low pass filter.

The transport in the baroclinic simulations also adjusts exponentially but on a much longer timescale, as displayed in the right panel of Fig. 5 for the model LN. We find a relaxation time $t_{\text{clin}} = 5{,}780$ days. From the wave analysis of BARBI (see Appendix 2) and the timescales in Table 2, it is evident that, now, the baroclinic Rossby waves participate in setting this long timescale, in cooperation with advective and viscous-diffusive effects. Clearly, the fast barotropic response is effective in the baroclinic system as well (high-frequency oscillations appear in the initial phase but are filtered in the figure by taking a large sampling time step) so that the transport is always adjusted on a timescale of days to the windstress and the baroclinic forcing acting at the moment. In the momentum balance (12), this is the pressure gradient conveyed by the potential energy; in the vorticity balance (1), it is the JEBAR torque. The transport in model version LN compares well with observations of the Drake Passage transport of 134 ± 13 Sv (see, e.g., Rintoul et al. 2001; Olbers et al. 2004), but in fact, this value has been tuned by choosing appropriate model parameters: It can easily be tuned by K or N because the steady state transport is governed by the eddy diffusion Kf^2/N^2 and not by viscosity (see Section 2 and Olbers et al. 2006).

The long baroclinic timescale calls for an extension of the Wearn–Baker model. Equation 6 can be viewed as a parameterization of the mean zonal momentum balance of the current between input of eastward momentum by windstress and export to the solid earth by

Table 2 Timescales arising from friction, diffusion and wave propagation

	Lat. friction B^2/A_h	Diffusion B^2/K	Advective L/u	Clin wave L/c_{clin}	Trop wave L/c_{trop}
Timescale (days)	233 (14.5)	5,790 (362)	4,630	2, 315	22

The parameters are those of the BARBI model. The current velocity is assumed $u = 0.05\text{ms}^{-1}$, the group velocities are evaluated as $c_{\text{trop}} = 10\ \text{ms}^{-1}$, $c_{\text{clin}} = 0.1\ \text{ms}^{-1}$. These are topographic wave speeds taken from a WKB wave analysis in Appendix 2 Waves, using moderate topographic slopes. The length B is taken here as width of the current, 1,000 km for the baroclinic case or 250 km for the barotropic case (in brackets); for the advective and wave adjustment the circumpolar length $L = 20{,}000$ km is considered

bottom formstress (see, e.g., Rintoul et al. 2001; Olbers et al. 2004, 2006),

$$\frac{\partial \bar{U}}{\partial t} = \bar{\tau}^x - h\overline{\frac{\partial P}{\partial x}} \tag{7}$$

where the overbar denotes the zonal mean. The bottom formstress builds up by propagation of planetary–topographic Rossby waves, generated by the zonal flow crossing the submarine topographic barriers and adjusting to them by friction (see Olbers et al. 2006, 2007). The formstress in the barotropic state relates to the zonal transport, and with $\bar{U}B \sim T$ and $\overline{hP_x} \sim \bar{U}/t_T$ with appropriate geometric scales (essentially the width B of the current), we obtain Eq. 6. This is the scenario of Charney and DeVore (1979), which originally applies to barotropic conditions. In a baroclinic system, however, the formstress includes a barotropic *and* a baroclinic component (see, e.g., Olbers and Völker 1996; Völker 1999). The pressure Poisson equation implies approximately $\nabla \cdot h\nabla P = f\nabla^2\psi - \nabla^2 E$, and thus, it seems reasonable to relate the bottom formstress in addition to the transport also to the baroclinic potential energy. A more complete linear model of barotropic and baroclinic variables is then of the form

$$\begin{aligned} \dot{T} + aT + bC &= mF \\ \dot{C} + cT + dC &= nF \end{aligned} \tag{8}$$

where we take $C = \Delta E/f = (E_n - E_s)/f$ as representation of the baroclinic variable[2] and F as a proper measure of the zonal windstress τ^x, e.g., a zonal mean at the latitude of Drake Passage. The matrix (a, b, c, d) describes the linear response to the forcing, and m and n are parameters measuring the strength of the forcing in the appropriate balance. The balance of transport in Eq. 8 follows the zonal balance (7) of zonal momentum; hence, the forcing in the first arises from the zonal windstress and thus $m \sim B$. Furthermore, the parameterization of the bottom formstress implies $a \sim b$. The baroclinic equation in Eq. 8 may be motivated by the balance of potential energy in the form (2). Hence, the forcing in the second equation arises from the windstress curl, and we get estimates for the parameters c, d and n directly by suitable scaling (not parameterization) of Eq. 2. This yields $n \sim \lambda^2/B$, $d = c \sim -f\lambda^2/B^2$. According to Eq. 8, the spin-up of $T(t)$ is now governed by the two eigenvalues of the matrix (a, b, c, d) with the trace $\theta = a + d \approx a$ and the determinant $\delta = ad - bc \approx d(a - b)$; hence, $\lambda_\pm = -(\theta/2)(1 \pm \sqrt{1 - 4\delta/\theta^2})$ results in $\lambda_+ \approx -a$, $\lambda_- \approx -d(1 - b/a)$. The response of $T(t)$ is hence governed by $1/a \sim t_{trop}$ on the short term and by the timescale $a/((a - b)d) \sim t_{clin}$ of the baroclinic field on the long term, as shown in Fig. 5.

[2]The indices n and s refer to northern and southern points in the model's Drake Passage.

5 Variability and trends from 1975 to 2005

The time history of the transport $T(t)$ for the NCEP wind and model version LN is displayed in Fig. 6 and compared with measurements collected on the World Ocean Circulation Experiment (WOCE) section SR1 across Drake Passage by Cunningham et al. (2003, Table 1) and Cunningham and Pavic (2007). The early observations from 1975 to 1980 are transport estimates relative to 3,000 dbar and thus considerably less than the above-mentioned mean value of 134 Sv for the absolute transport through Drake Passage. We have shifted the mean of these early data to the mean of the time series of Cunningham and Pavic (2007) who estimate absolute transports through Drake Passage for each year from 1993 to 2003 from the section data, satellite altimetry, and current measurements. Their mean is 137.1 Sv, and the standard deviation is 6.9 Sv. There is a bias in these section data toward the Austral summer. On the SR3 section between Tasmania and Antarctica, Rintoul et al. (2002) find a similar standard deviation (their transport estimate is 147 ± 6.1 Sv) from six repeats from 1991 to 1996 distributed more evenly over the seasons. The values for the BARBI experiment are 144.4 Sv for the mean and 13.7 Sv for the standard deviation. The variability of BARBI is thus considerably more intensive than the observed variability (but note that we compare a transport record with a sampling step of 7 days for 30 years

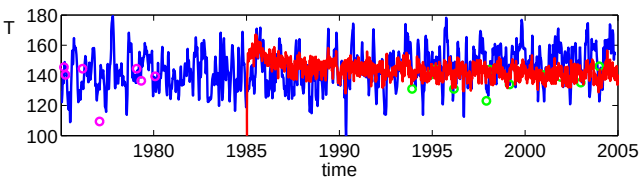

Fig. 6 Transport through Drake Passage from 1975 to 2005. The *magenta circles* mark the measured values listed in Table 1 of Cunningham et al. (2003) for hydrographic sections taken from 1975 till 1980. The *green circles* are yearly estimates from 1993 till 2003 from WOCE sections according to Cunningham and Pavic (2007). The *blue curve* is the BARBI transport with a sampling time of 7 days, the *red curve* is the Drake Passage transport from the OCCAM model (5-day mean values). The section data 1975–1980 (*magenta circles*) have been shifted to the same mean as the section data 1993–2003

daily forcing with a few section data). The standard deviations of transport derived from pressure differences across the ACC in Drake Passage, as reported by Meredith et al. (1996) from 10-day filtered data, have a higher temporal resolution and range from 5.3 to 8.9 Sv.

Figure 6 also shows the Drake Passage transport from the numerical eddy resolving model OCCAM (B. De Cuevas, personal communication; it is the 1/4° model; Webb et al. 1998). OCCAM was forced by six hourly NCEP winds from 1985 to 2004. As a side note, we mention that adjustment timescale of the OCCAM transport, visible in Fig. 6, has a similar size as the baroclinic timescale of BARBI (cf. Fig. 5). The mean transport in OCCAM, 143.5 Sv, is of similar size as the section data and the result from BARBI. Its standard deviation 6.9 Sv (from 5-day mean values) is low, and we have to face that BARBI may have a too large variability. In contrast to OCCAM, the Modeling Eddies in the Southern Ocean (MESO) project (Hallberg and Gnanadesikan 2006) reports a much higher variability, a weekly peak-to-peak range of 30 Sv, although the experiments are forced by constant windstress. The 1-year low-pass-filtered transport in the 1/6° MESO model still varies by about 5 Sv. The comparison of the variability resulting from the simple BARBI model with the one simulated by eddy-resolving models as OCCAM or MESO thus leads to a note of caution. The variability arising from wind forcing seems to be less in these models than in BARBI, most likely because eddies behave more nonlinear than a diffusive eddy parameterization. In addition, the presence of (real or adequately resolved) eddies excites its own variability of transport that is not directly related to wind variations. Furthermore, eddies seem to produce at the same time a lower saturation limit for the variability. As we are mainly concerned with linear aspects—wave propagation and correlations of directly forced variability—we expect that the discrepancy between eddy resolved simulations and the coarse BARBI simulations is not a severe problem.

Applying a Student's *t*-test to the section data, Cunningham et al. (2003) conclude that the mean values (for the relative transport values) during the two periods 1975–1980 and 1990–2000 are different, but not at a significance level of 95%. A long-term trend cannot be derived from these measured transport values. The NCEP windstress, however, is clearly increasing over these 30 years. In the upper panels of Fig. 7, the NCEP zonal wind stress, spatially averaged between 68 and 47°S, shows a positive linear trend with an increase of 25.5% over the considered period. The BARBI model responds to the NCEP winds by a linear increase of

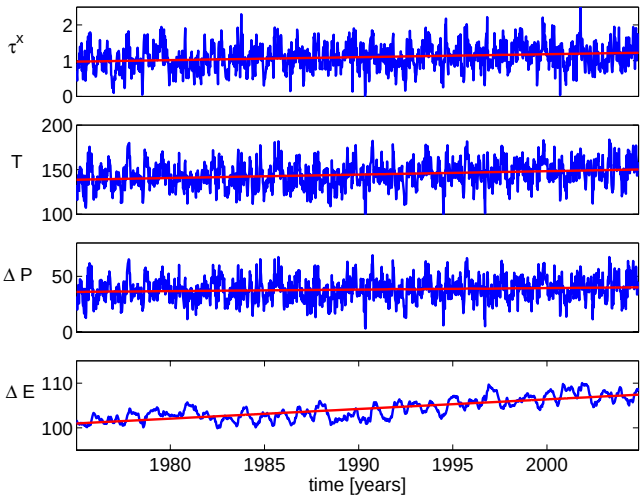

Fig. 7 *Upper panel* spatially averaged zonal wind stress between 68 and 47°S (units are 10^{-4} m^{2}s^{-2}). The *following panels* show the transport through the Drake Passage, the difference of bottom pressure across Drake Passage, converted to transport units by $-h_0(P_n - P_s)/f$ with $h_0 = 2{,}000$ m, and the difference of potential energy in the form $-(E_n - E_s)/f$ (the data are from model version LN). The data are unsmoothed with sampling step 7 days. The *red lines* are linear fits

transport by 8.2% (see second panel of Fig. 7). The figure also displays the difference of bottom pressure P and of potential energy E across Drake Passage, converted to transport values. The pressure gradient increases by 11.2%, and the potential energy gradient increases by 6.4% over the 30 years, respectively. Note however, that the potential energy rises mainly after 1990. There is a delay of roughly 10 years, which is consistent with the long response time of the baroclinic field. The comparison of the time history of E with the wind and P nicely demonstrates that E is indeed the slow component of a stochastically forced system in the sense of Hasselmann (1976).

In steady state, the ACC is in geostrophic balance, and on the basis of BARBI experiments, Olbers et al. (2006) have shown that pressure gradients associated with the potential energy E are dominating over gradient of the bottom pressure P in this balance. In fact, one finds the approximate relation $f\nabla\psi \sim \nabla E$ or $\psi \sim E/f$ over most of the Southern Ocean. The quantity $(1/f)\nabla E$ is approximately equal to the geostrophic transport relative to the bottom (see Olbers et al. 2006). This correspondence has also been suggested by Borowski et al. (2002). A reasonable proxy for the time-mean transport is the difference of E across Drake Passage, more specifically $T \simeq -(E_n - E_s)/f = -C$. For fluctuations, we have pointed out the long response time of the baroclinic field, and thus, the above relations should not hold for periods less than a few

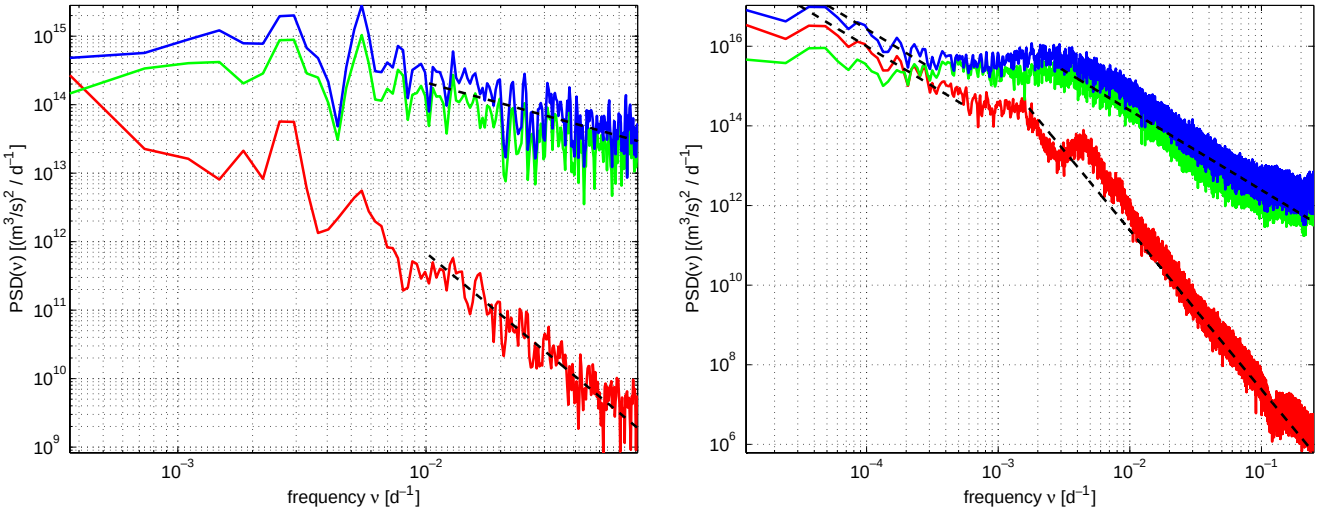

Fig. 8 Power spectral density of T (*blue*), $h_0(P_n - P_s)/f$ (*green*), and $(E_n - E_s)/f$ (*red*) for the NCEP (*left*) and AR (*right*) experiments, with $h_0 = 2{,}000$ m and $f = -1.2 \times 10^{-4}$ s^{-1}. The *straight lines* indicate various spectral slopes (see text). The outstanding peaks in the NCEP-forced simulation have annual and semiannual periods

years (smaller than t_{clin}). Figure 8 compares the power spectra of T, $h_0(P_n - P_s)/f$ and $C = (E_n - E_s)/f$ for the NCEP and AR experiments. These quantities have units m^{3}s^{-1}, and for an appropriately chosen depth h_0 for Drake Passage, the steady-state geostrophic balance would equate T to the (negative) sum of the two pressure gradients, with the E-term dominating. Although the NCEP resolution is just enough to speculate that the simulation approaches such a state, we see that the low-frequency domain of the AR simulation has reached it. At high frequencies, however, the P-term carries most of the variability of the geostrophic transport. The NCEP simulation shows annual and semiannual peaks in all spectra. The AR case has a clear impact from the forcing. For periods exceeding 500 days—the ramp period of the forcing as shown in Fig. 3—the T and $h_0(P_n - P_s)/f$ spectra flatten to a plateau, and while the latter continues for higher periods, the T spectrum picks up some redness again. This arises from the C part that increases right from the ramp frequency on to lower frequencies.

At frequencies above 0.1day^{-1}, there is a manifestation of the barotropic variability, clearly visible in the C-spectrum but also in the more energetic other two spectra. The marginal break of spectral slope at about 2×10^{-4}day$^{-1} \equiv 5{,}000$ days in the T-spectrum might be an indication of the baroclinic timescale. More spectacular are broad peaks in the C-spectrum at intermediate frequencies, most prominent at about 5×10^{-3}day$^{-1} \equiv$ 200 days but also appearing higher frequencies. It is hard to judge whether these latter peaks are harmonics of the previous peak (the potential energy balance is nonlinear) or whether they have independent values. Note that there is also some overshooting of spectral power in the T and P spectra before these settle to their respective plateau. As these peaks cannot arise from the forcing nor from the barotropic or baroclinic intrinsic adjustment, we suggest that these intermediate peaks are associated with resonant Rossby waves or partly or even fully developed baroclinic basin modes of the circumpolar system. The maximum period of baroclinic topographic Rossby waves are typically 100 to 200 days (cf. Appendix 2).

Due to these broad band peaks at intermediate frequencies, it is hard to extract a power law behavior for the high-frequency range. The power spectral densities of T and $h_0(P_n - P_s)/f$ have a similar behavior, whereas $(E_n - E_s)/f$ is much 'redder'. In Fig. 8, we show various spectral slopes. For the high- and the low-frequency T spectrum of the AR simulation, a -2 slope is included, whereas for the high-frequency E spectrum, a -4 slope. The corresponding slopes for the NCEP simulations are -1 and -3, respectively.

6 Correlation patterns

Several studies (see, e.g., Hughes et al. 1999, 2003; Aoki 2002; Meredith et al. 2004; Vivier et al. 2005) have shown that the bottom pressure in the south of Drake Passage and, more generally, along the Antarctic continental shelf reflects the oscillations in transport through Drake Passage. This result is strongly supported by the BARBI experiments as well. Figure 7 demonstrates, for model version LN and real winds (NCEP wind forcing), a very high correlation between the transport and the

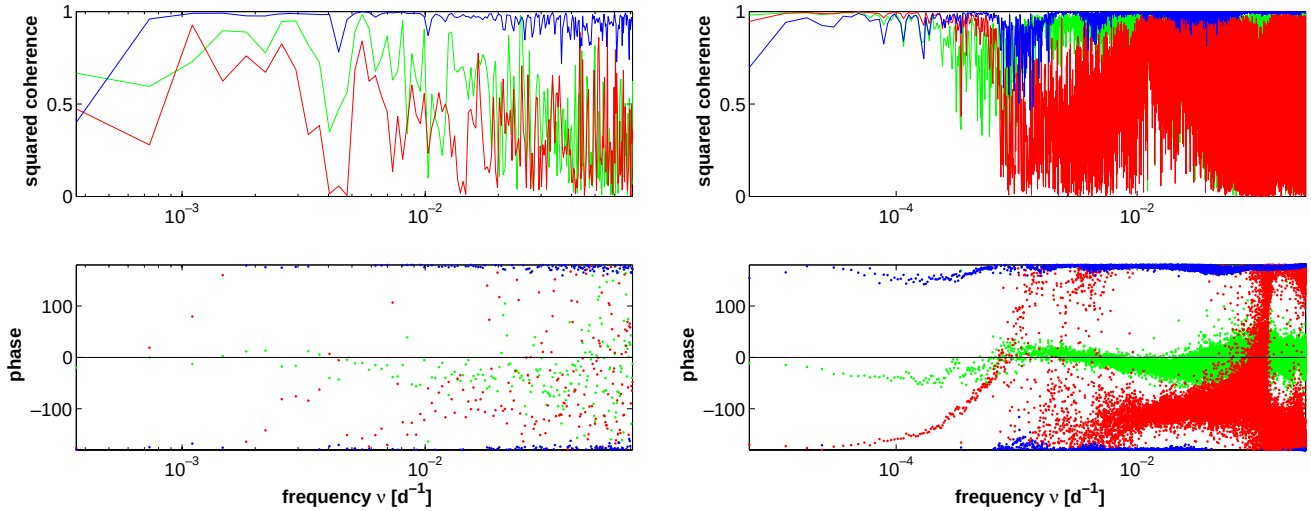

Fig. 9 Coherence and phase between transport through Drake Passage and various quantities: the difference $(P_n - P_s)/f$ of bottom pressure across Drake Passage (*blue*), the meridional difference $(E_n - E_s)/f$ of potential energy (*red*), and the mean zonal windstress τ^x (*green*), for NCEP winds (*left panels*) and the artificial AR wind forcing (*right panels*)

bottom pressure gradient across Drake Passage; the correlation coefficient in this example is 0.9 with a sampling time step of 7 days. Figure 9 (left panels) shows the coherence and phase of the ACC transport with the mean zonal wind, with the pressure difference $(P_n - P_s)/f$, and with $C = (E_n - E_s)/f$ for periods less than a year (obtained with NCEP forcing). The coherence between T and the bottom pressure P_s in the south of Drake Passage is not shown; it is slightly less than the one with pressure difference. Transport and windstress are highly correlated for periods above a few months. Their phase lag is negative indicating a lead of the wind as in the result of Wearn and Baker (1980) and previously cited more extended studies. The coherence with the bottom pressure is at high levels for the entire interval of periods, whereas the one with the potential energy gradient remains quite small. The phases between T and the pressure difference are consistent with a geostrophic balance for periods approaching 1 year. The phase of T and C remains indifferent at these low periods.

The situation changes if longer periods are considered. The right panels of Fig. 9 display the coherence and phase, now calculated from the simulations with the artificial AR windstress. The coherence between transport and potential energy increases toward larger periods to values that exceed the coherence with the wind forcing and the one with the bottom pressure. Again, the phase relations in the low-frequency range indicate an approach toward a geostrophic balance. As can be seen in the spectra of Fig. 8 as well, the baroclinic field clearly dominates the low-frequency variability of the system. All AR-simulated fields have a loss of coherence in frequency range of about 10^{-3} to 10^{-2}day^{-1} (equivalently 1,000 to 100 days), most dramatically appearing in the baroclinic field. A shift of phase by 360° is accompanying its coherence drop. This is the interval where the peaks occur in the spectra (see Fig. 8).

Proceeding from these local correspondences between transport, pressure, and forcing, we show in Fig. 10 the correlation of the bottom pressure, potential energy, windstress, and windstress curl in the entire Southern Ocean with the transport through Drake Passage for different wind scenarios. The upper row uses NCEP forcing for 30 years; the middle and bottom rows have the AR wind forcing. The middle correlations are based on a record with 2,000 days sampling rate, and the bottom correlations use a low-pass filter of 25 years.

Consistent with the discussion in Section 2 and earlier studies, the highest correlations in the pressure simulated by BARBI are found in the f/h tunnel near the coast of Antarctica. They are negative and close to −1. More to the north, the correlations become smaller, but we notice that the excursions of high correlations proceed above topographic feature that extend from Antarctica to the north, especially at the Kerguelen Plateau, the Pacific–Antarctic Ridge, and the region of the Scotia Basin, east of Drake Passage. In congruence to the findings of Vivier et al. (2005), the excursions of high correlations are not symmetric on the ridges; they are intensified on the eastern flanks. A marked difference between NCEP and AR forcing is the filament of negative correlation reaching up the Argentine Basin. Northward of the f/h tunnel region, the correlation is positive, with values as high as 0.5 over large regions.

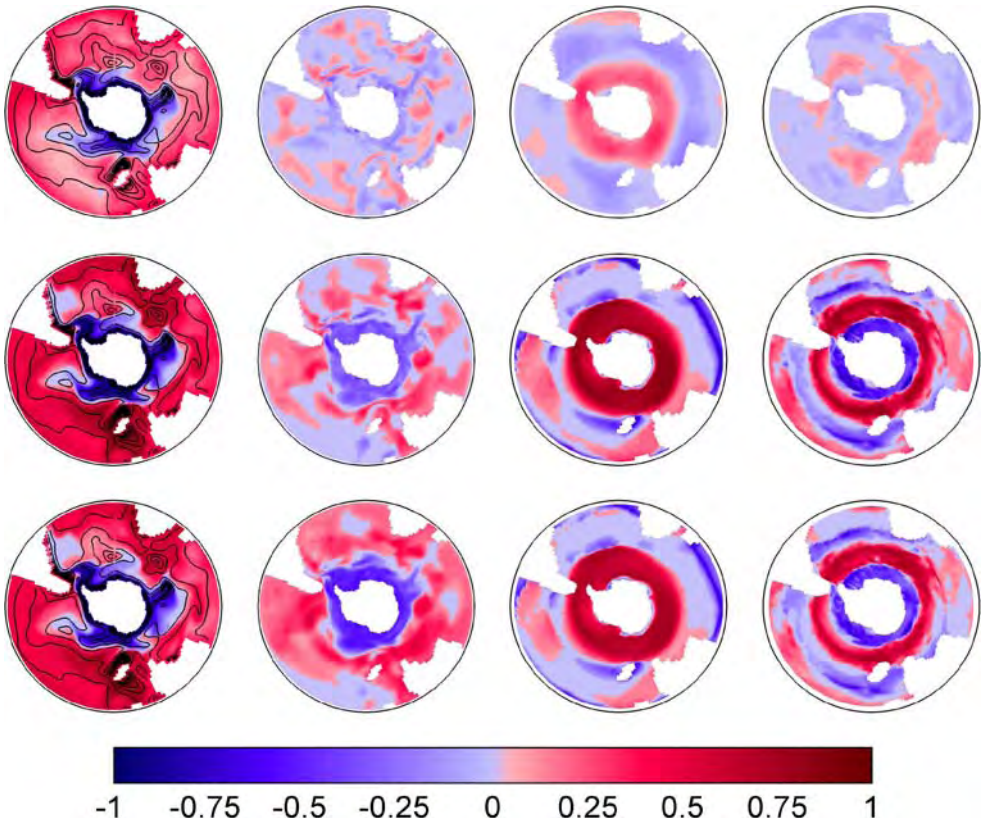

Fig. 10 *Upper row* correlation between transport through Drake Passage and various fields for model version LN and NCEP winds. *From left to right* with bottom pressure, potential energy, zonal windstress, and curl of windstress. *Middle row* same for the AR wind experiment. These data are sampled with time step 2,000 days. *Lower row* same for the AR wind experiment. These data are low-pass filtered with cutting period of 25 years. The f/h contours are depicted in the *leftmost panels*

The entire pattern of pressure correlations becomes slightly more pronounced in the AR cases. This may be due to a larger regional coherence of the AR forcing data compared to NCEP.

Correlations with the other relevant fields in the NCEP forcing are significantly lower (see the low correspondence of transport and potential energy in Fig. 7 and the results in the panels of the upper row of Fig. 10). The potential energy has a correlation level of about 0.2 maximum with positive and negative values oriented at the gradient of the topography as suggested by the driving of barotropic vorticity via the JEBAR torque. A quite patchy picture results this way. Correlations with the zonal windstress reflect the SAM pattern, a belt with positive values of about 0.4 maximum in the strong wind area, and correlations with the wind curl are much lower and apparently have some modulation by the large-scale ocean ridge systems.

The correlation patterns change quite significantly when the experiment with AR forcing is considered. At first, not surprisingly, the transport–wind correlations increase and clearly show the circumpolar SAM pattern with coefficients close to one. There is a slight decrease in the maximum values from the 2,000-day sampling case to the 25-year low-pass case. In contrast, the transport–potential energy correlation increases steadily from NCEP to the more and more low-pass versions with AR winds. Moderately high negative values occur in the tunnel area, being congruent with the P-pattern but less significant. Positive values are found more to the north, spread over the entire model domain, and not at all structured by the SAM pattern or the f/h pattern. In the extremely filtered case (lowest row), the correlations are highest, 0.7 maximum. The highest values are found in large areas in the western Pacific (west of the Pacific Ridge), south of Australia (north of the Southeast Indian Ridge), on the eastern flank of the Midatlantic Ridge, and on the ridge system south of Africa. These areas have been identified by Vivier et al. (2005) as 'resonant regions'. In these regions, closed f/h contours are found (see Fig. 1).

7 Regression and stochastic dynamical models of the transport variability

Linear regression models confirm the ranking of barotropic and baroclinic fields with respect to the timescales of variability. Consider

$$T^r(t) = \alpha\mathcal{A}(t) + \beta\mathcal{B}(t) + \gamma\mathcal{C}(t) + \ldots \quad (9)$$

where $\mathcal{A}$, $\mathcal{B}$, $\mathcal{C}$, ... are observed properties (predictors), e.g., bottom pressure or wind stress at a certain place in the model domain, and α, β, γ, ...are the regression

Table 3 Overview over the four different regression models and the absolute values of the resulting correlation coefficients (two rightmost columns) between the transport $T(t)$ of the BARBI simulation and the predictant $T^r(t)$

Model	P_s	$\Delta E/f$	τ^x	NCEP wind	AR wind
A	+			0.903	0.891
B		+		0.204	0.979
C			+	0.649	0.864
D	+	+	+	0.924	0.995

A + indicates whether this variable was used in the regression model as predictor.

coefficients that are to be adapted to the data to obtain an optimal value for the predictant T^r of the transport. The regression coefficients are determined as least-squares solution of the problem $||T^r(t) - T(t)|| = \min$ where $T(t)$ is the BARBI transport. We studied various regression models, differing in the data combination for the predictors and the length of the BARBI model integrations and the applied windstress forcing (see Table 3).

The results of the regression model, applied to the BARBI experiment with the NCEP wind and model version LN, are displayed in the left block of panels of Fig. 11. The sampling interval for the time series is 3 days. The potential energy data are taken from Drake Passage, the bottom pressure in the south, and the wind stress is the zonal mean at the latitude of Drake Passage. The figure shows anomalies (the mean values are subtracted) of the BARBI transport (blue curves) and the transport of the four regression models (red curves). It is obvious that bottom pressure reflects the transport very well (case A), whereas the local wind stress in the Drake Passage has a marginal skill (case C), and the difference of potential energy (case B) is not at all suited to describe the variability of Drake Passage transport on these short timescales. A slightly higher skill can be seen if all three predictors are used (case D). Longer timescales are considered in the right block of panels of Fig. 11. Wind type AR is applied, and the time series are low-pass filtered with a cutting period of 50 years to eliminate the short-time variability before the regression procedure is applied. Of all single predictor data, the potential energy is clearly most successful to model the transport. The regression on all three data fields is perfect.

In summary, the regression models confirm that the bottom pressure reflects the transport on shorter than decadal timescales, whereas longer periods are better captured in the baroclinic potential energy.

Apart from physically motivated preferences of the applied data concerning the timescale of variability, the previous regression models are purely statistical. The final study of transport variability is based on the dynamical model (8), interpreted now as a stochastic model for the deviations of the quantities T, C and $F = \tau^x$ from the mean state. For the high-frequency barotropic case, a similar approach is discussed in Sura and Gille (2003) and in Weijer and Gille (2005). Sura and Gille (2003) derived the linear Wearn–Baker

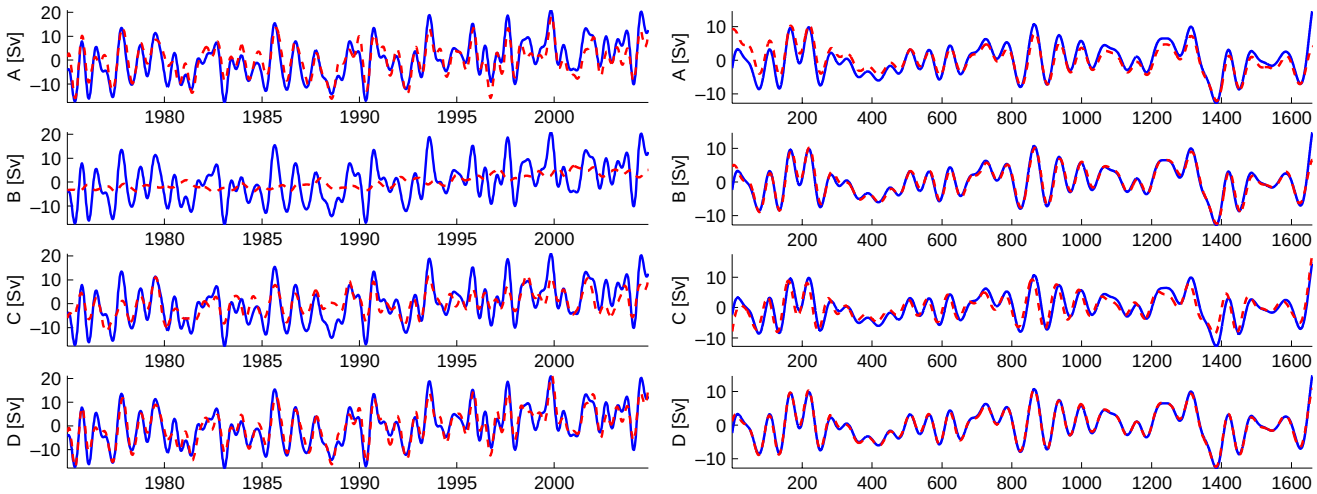

Fig. 11 Time series of transport anomaly through Drake Passage for the short NCEP forcing (*left*) and long AR forcing (*right*) experiments. *Blue* BARBI transport, *red* transport of the corresponding regression models for types A to D

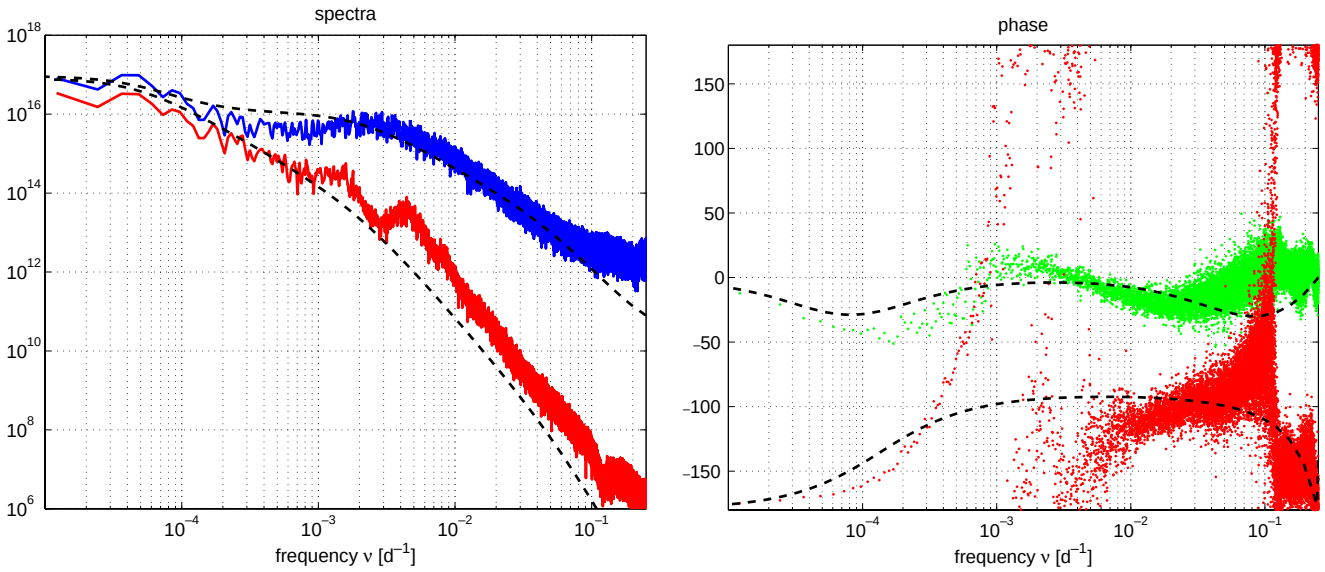

Fig. 12 *Left* power spectra of T (*blue*) and C (*red*) from the AR experiment and corresponding model spectra from the stochastic model (*black*). *Right* phase between T and F (*green*) and between T and C (*red*) and corresponding model phases from the stochastic model (*black*). The parameters are $1/a = 2$ days, $b = 0.7a$, $1/d = 1{,}000$ days, $c = d$, $m = B = 1{,}000$ km, $n = \lambda^2/B$. The stochastic model takes into account that the data have a finite sampling δt, i.e., ω in Eq. 11 must be replaced by $i(\exp(-i\omega\Delta t) - 1)/\Delta t$

model (6) from a general stochastic nonlinear Itô-equation, using wind and bottom pressure data. Weijer and Gille (2005) applied Eq. 6 in the frequency domain, using data from a wind-driven barotropic Southern Ocean model. From the coherence of the Wearn–Baker model, they estimate a barotropic timescale of 3 days, which is much smaller than the spin-up scale discussed in Section (4). Our more complete stochastic model (8) yields a similar result.

We proceed by considering the behavior of the model in the frequency domain. First T and C are mutually eliminated,

$$\begin{aligned} \ddot{T} + \theta\dot{T} + \delta T &= m\dot{F} + \tilde{m}F \\ \ddot{C} + \theta\dot{C} + \delta C &= n\dot{F} + \tilde{n}F \end{aligned} \tag{10}$$

with $\theta = a + d, \delta = ad - bc, \tilde{m} = md - nb$, and $\tilde{n} = na - mc$, revealing that the barotropic and the baroclinic variables are governed by the same temporal response operator. The forcing, however, distinguishes the variables. The Fourier transformation of Eq. 10 yields

$$\begin{aligned} \hat{T}(\omega) &= \left(\frac{\tilde{m}(\delta-\omega^2)+\omega^2 m\theta}{(\delta-\omega^2)^2+\omega^2\theta^2} - i\omega\frac{m(\delta-\omega^2)-\tilde{m}\theta}{(\delta-\omega^2)^2+\omega^2\theta^2} \right) \hat{F}(\omega) \\ \hat{C}(\omega) &= \left(\frac{\tilde{n}(\delta-\omega^2)+\omega^2 n\theta}{(\delta-\omega^2)^2+\omega^2\theta^2} - i\omega\frac{n(\delta-\omega^2)-\tilde{n}\theta}{(\delta-\omega^2)^2+\omega^2\theta^2} \right) \hat{F}(\omega) \end{aligned} \tag{11}$$

where $\omega = 2\pi\nu$ is the angular frequency. Spectra and cross-spectra of T, C and F are readily evaluated as function of the basic parameters. The skill of the model is exemplified in Fig. 12 for a reasonable choice of parameters (a elaborate fit is not attempted) and a model wind spectrum $\sim (\omega^2 + \omega_0^2)^{-1}$ fitting the AR windstress spectrum from Fig. 3 with $2\pi/\omega_0 = 500$ days. The stochastic model is clearly a reasonable description of the variability, of course excepting the complicated peak structure at intermediate frequencies, which has been discussed above and attributed to resonant basin modes. In fact, the stochastic model may serve as a model of the background variability.

8 Summary

The relative short temporal range of ocean observations hinders the investigation of low-frequency variability of the ACC transport, and it is not surprising that most statements of the present investigation are based on model results and a verification by direct observations has yet to wait. We have analyzed simulations of the Southern Ocean circulation, in particular the resulting ACC transport variations, by a simple wave model driven either by a wind product of observed quality or by artificial but realistic wind data over timescales of many centuries. We use the BARBI model of Olbers and Eden (2003) truncated to two modes with topographically modified barotropic and

baroclinic Rossby waves being in center of the current study.

Our main findings are:

- The 'Southern Mode' of variability with coherence between ACC transport, Southern Ocean windstress, and bottom pressure all around Antarctica extends to periods well above decadal, with baroclinic processes coming into play. Baroclinic Rossby waves, not bound to f/h contours, spread coherent signals across the entire Southern Ocean, and the baroclinic potential energy—as manifestation of the baroclinic pressure—takes control of the ACC transport.
- The spin-up to steady state and the variability in the spectral window from daily to centennial periods can be represented by a simple two-dimensional linear response model, extending the Wearn–Baker model to long periods. The response model can be viewed as an example of Hasselmann's stochastic climate model (Hasselmann 1976), with the ACC transport as fast variable, the baroclinic pressure gradient across Drake Passage as the slow variable, and the windstress as red noise forcing. The timescales of the model differ drastically for the fast variable (a few days; 2 days for our model) and the slow variable (a few years; 1,000 days for our model).
- Simulations with observed windstress fields from NCEP have a higher variance of transport fluctuations than those inferred from hydrographic data or calculated from bottom pressure records. The model follows the positive trend of the windstress (about 25% over 30 years) by a disproportional increase of the ACC transport (by 8% over 30 years).
- In an intermediate range between about 100 and 1,000 days, low-frequency broad peaks were found, mainly in the spectrum of baroclinic potential energy, perturbing the coherence and phase relations of the otherwise simple linear stochastic model that therefore may serve to define the unperturbed background variability. These peaks are likely associated with baroclinic topographic Rossby waves, either resonantly excited in a local dissipative balance or even developed in a basin mode stage.

A few words of caution are appropriate. Some of the findings, in particular with respect to behavior at very low frequencies, depend on our artificial windstress. It is constructed to reflect the SAM with its high spatial coherence at low frequencies. Real winds might show less coherency, and the resulting correlation patterns of transport, wind, and pressure might degrade. A similar effect could arise if higher baroclinic modes and/or realistic eddies are admitted. With this in mind, we value our results as a strawman against which more complex models or more realistic forcing fields could be tested.

Acknowledgements We appreciate numerous discussions with Sergey Danilov. We are grateful to the encouraging and very helpful comments of two anonymous reviewers.

Appendices

1 The BARBI model

Our model is a two-mode version of the reduced physics model BARBI ocean model (Olbers and Eden 2003) and can be summarized by the set of equations

$$\frac{\partial \mathbf{U}}{\partial t} + f\mathbf{k}\times\mathbf{U} = -h\nabla P - \nabla E + \boldsymbol{\tau} + A\nabla^2\mathbf{U} \tag{12}$$

$$\frac{\partial \tilde{\mathbf{u}}}{\partial t} + f\mathbf{k}\times\tilde{\mathbf{u}} = \frac{1}{3}h^2\left[\nabla E - \tau\right] \tag{13}$$

$$\nabla\cdot\mathbf{U} = 0 \tag{14}$$

$$\frac{\partial}{\partial t}E + h\mathbf{U}\cdot\nabla\frac{E}{h^2} - \frac{1}{2}N^2\nabla\cdot\left[\tilde{\mathbf{u}} + \frac{1}{3}\mathbf{U}h^2\right] = \mathcal{Q} - \mathcal{D}[E] + K\nabla^2 E \tag{15}$$

with $\tilde{\mathbf{u}} = \mathbf{u}_2'$, $E = E_1$ in the notation of Olbers and Eden (2003). Equation 12 is the vertically integrated balance of momentum with a simplified viscous term,

$$\mathbf{U} = \int_{-h}^{0}\mathbf{u}\,\mathrm{d}z \tag{16}$$

is the vertically integrated velocity, h is the ocean depth, P is the bottom pressure, and $\tilde{\mathbf{u}}$ is the second vertical moment of the baroclinic velocity $\mathbf{u} - \mathbf{U}/h$. The mass balance (14) allows to represent $\mathbf{U}$ by the streamfunction of the volume transport, $\mathbf{U} = \mathbf{k}\times\nabla\psi$. Equation 15 is the balance of baroclinic potential energy

$$E = g\int_{-h}^{0} z\rho\,\mathrm{d}z \tag{17}$$

where ρ is a perturbation density about a mean background stratification (and scaled by a constant reference density) described by the Brunt–Väisälä frequency N. The latter is taken constant in this study.

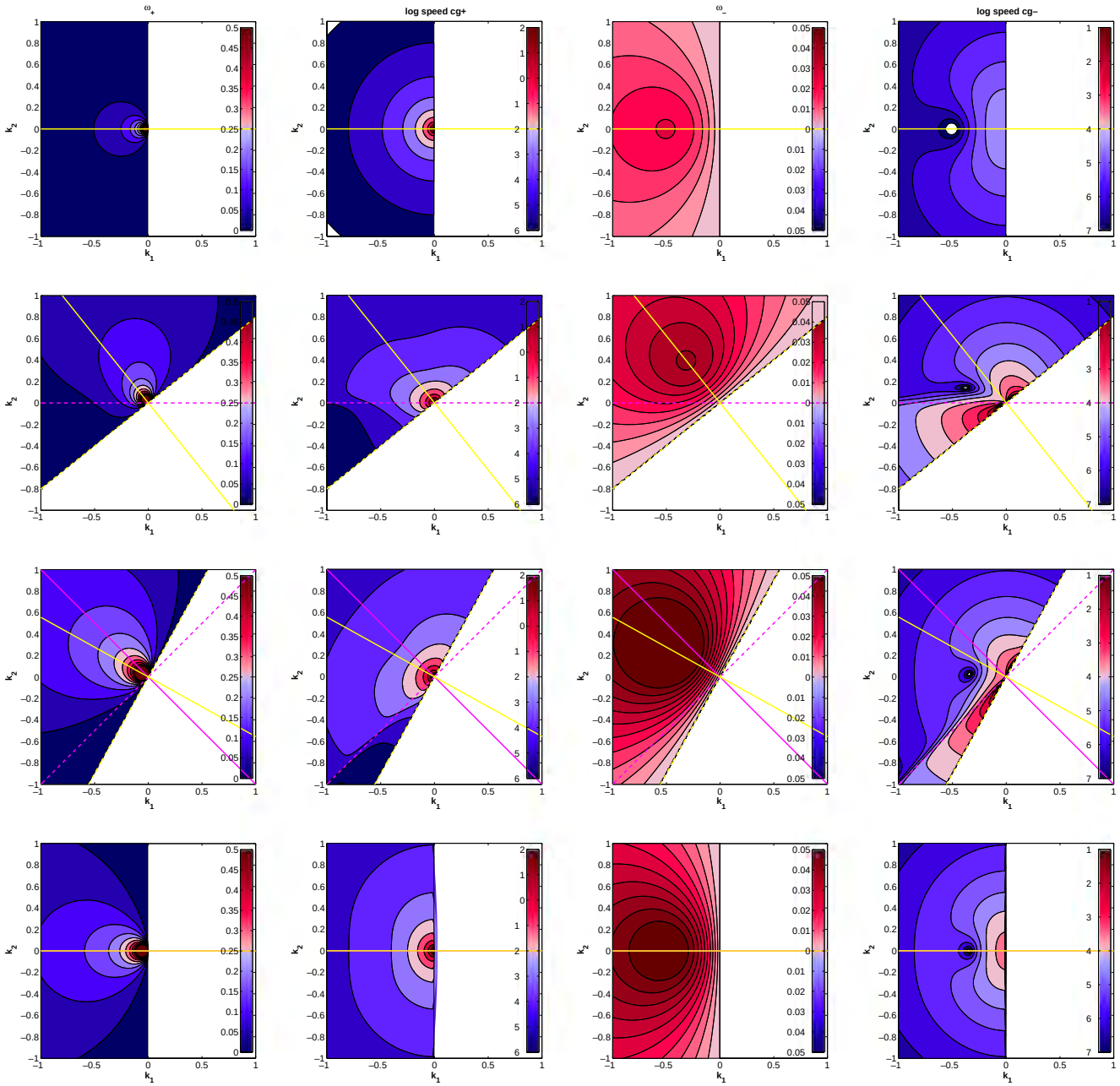

Fig. 13 Dispersion relation and group velocity (speed). *Left two panels in each row* show the +solution, *right two panels* show the −solution. *Upper row* for flat bottom. *Lower rows* for $\nabla h = (n, m) \times 10^{-3}$ for $nm = 10, 11$ and $nm = 01$. The *graphs* show only the functions in the halfplane with positive wavenumber along $f/h = \text{const}$. The *axes* are scaled by $K_{\max} = 2/\lambda$. The frequency is in cpd, the maximum for +solution is 0.5 cpd, for −solution 0.05 cpd. The logarithmical of group velocity in m s^{-1} is displayed. The range for the +solution is $10^{-6} \cdots 10^{2}$m s^{-1}, for the −solution $10^{-7} \cdots 10^{-1}$m s^{-1}. The *yellow cross* is oriented at $\nabla(f/h)$, the *purple cross* at ∇h (the *dashed lined* are along the gradients, the *full lines* are along $f/h = \text{const}$ and $h = \text{const}$, respectively)

The potential energy balance has a prescribed source function $\mathcal{Q}$, and $\mathcal{D}[E]$ represents dissipation. We use a damping form $\mathcal{D} = \mu E$. The diffusive term in Eq. 15 together with the dissipation can be derived from a Gent–McWilliams parameterization of the eddy-induced density advection. This is outlined in Olbers et al. (2006).

As a consequence of the rigid-lid approximation, the bottom pressure is a diagnostic variable that is determined by a Poisson equation,

$$\nabla \cdot h \nabla P = -\nabla^2 E + f\nabla^2 \psi + \beta \frac{\partial \psi}{\partial y} + \nabla \cdot (\boldsymbol{\tau} + A\nabla^2 \mathbf{U}) \quad (18)$$

This equation is used to compute P in BARBI.

We like to point out that most terms in the above balances result exactly by vertical integration of the primitive equations. However, the BARBI system has a closure to utilize $\mathbf{U}$, E and $\tilde{\mathbf{u}}$ as a complete set of state variables. The closure mainly concerns the baroclinic pressure term in Eq. 13. For details, we refer to Olbers et al. (2006) and only mention here that the Brunt–Väisälä frequency in Eq. 15 is an effective one related to the true one N_0 by $N_0 = \pi N/\sqrt{6}$. The relation ensures that the first baroclinic Rossby radius $\lambda = Nh/|f|/\sqrt{6}$ of the above system equals the familiar form $\lambda = N_0 h/(|f|\pi)$.

The numerical implementation of BARBI is very similar to MOM (most code fragments have actually been taken from MOM), e.g., finite differences in space and time are second order, an Arakawa B-grid is used, coding is in FORTRAN 90. The topography is interpolated on the grid corresponding to a 'partial cell' implementation.

2 Waves

We look for a WKB solution with the ansatz $(f\psi, E) \sim \mathbf{R}\exp i(\mathbf{K}\cdot\mathbf{x} - \omega t)$ with wave vector $\mathbf{K} = (k, \ell)$ and eigenvector $\mathbf{R}$ (polarization vector). A wave with $\mathbf{R} = (1, 0)^T$ is barotropic and with $\mathbf{R} = (0, 1)^T$ baroclinic. The gradients $\boldsymbol{\alpha} = \nabla h$, $\boldsymbol{\beta} = (0, \beta)$, and $\boldsymbol{\gamma} = \nabla(f/h)$ are assumed constant in a WKB sense. Note that $\boldsymbol{\gamma} = -(f/h^2)\boldsymbol{\alpha} + \boldsymbol{\beta}/h$. The complete model with prognostic baroclinic momentum balance (13) possesses the familiar baroclinic gravity waves. For simplicity, we filter gravity waves but not short baroclinic Rossby waves. This is achieved by canceling the tendency term in Eq. 13. The wave problem is then given by the vorticity balance and the linearized balance of potential energy. We get

$$(1-R^2\nabla^2)\frac{\partial f\psi}{\partial t} + hR^2\,\underset{\neg}{\boldsymbol{\gamma}}\cdot\nabla f\psi + \frac{f}{h}R^2\,\underset{\neg}{\boldsymbol{\alpha}}\cdot\nabla E = 0 \quad (19)$$

$$(1-\lambda^2\nabla^2)\frac{\partial E}{\partial t} + \lambda^2\left[h\,\underset{\neg}{\boldsymbol{\gamma}} - \frac{f}{h}\,\underset{\neg}{\boldsymbol{\alpha}}\right]\cdot\nabla E + 2\lambda^2\frac{f}{h}\,\underset{\neg}{\boldsymbol{\alpha}}\cdot\nabla f\psi = 0 \quad (20)$$

where a rotated vector notation is used: $\underset{\neg}{\boldsymbol{\gamma}} = (-\gamma^y, \gamma^x)$ is the rotated vector of $\boldsymbol{\gamma} = (\gamma^x, \gamma^y)$ (anticlockwise by $\pi/2$). We have introduced the term with the external Rossby radius $R = \sqrt{gh/f^2}$ for completeness. Inserting the wave ansatz yields

$$\begin{pmatrix} \omega-\omega_R & \omega_T \\ 2\omega_A & \omega-2\omega_A-\omega_C \end{pmatrix}\begin{pmatrix} f\psi \\ E \end{pmatrix} = 0 \quad (21)$$

The frequencies ω_T and ω_A describe pure topographic waves, ω_R is a mixed barotropic topographic–planetary wave, and ω_C the flat-bottom baroclinic Rossby wave. They are given by

$$\omega_T = -\frac{fR^2}{h}\frac{\mathbf{K}\cdot\underset{\neg}{\boldsymbol{\alpha}}}{1+K^2R^2} \qquad \omega_A = -\frac{f\lambda^2}{h}\frac{\mathbf{K}\cdot\underset{\neg}{\boldsymbol{\alpha}}}{1+\lambda^2K^2}$$

$$\omega_R = hR^2\frac{\mathbf{K}\cdot\underset{\neg}{\boldsymbol{\gamma}}}{1+K^2R^2} \qquad \omega_C = -\frac{\beta\lambda^2 k}{1+\lambda^2K^2}$$

Note that $\omega_R = \omega_T + \omega_P$ and $\omega_L = \omega_A + \omega_C$ where

$$\omega_P = -\frac{\beta R^2 k}{1+K^2R^2} \qquad \omega_L = h\lambda^2\frac{\mathbf{K}\cdot\underset{\neg}{\boldsymbol{\gamma}}}{1+K^2\lambda^2} \quad (22)$$

are associated with the flat-bottom barotropic planetary wave and the mixed baroclinic mixed topographic–planetary wave, respectively.

Barotropic case For $\lambda = 0$, we find $E \equiv 0$ and $\omega = \omega_R$ as the only solution. This is the barotropic mixed topographic–planetary Rossby wave. Note that the group velocity of long waves, $(KR)^2 \ll 1$, is along f/h contours.

Flat bottom case In this study, the vorticity and potential energy balance are decoupled, so that we find $\omega_1 = \omega_P$ and $\omega_2 = \omega_C$ with eigenvectors $\mathbf{R}_1 = (1, 0)^T$,

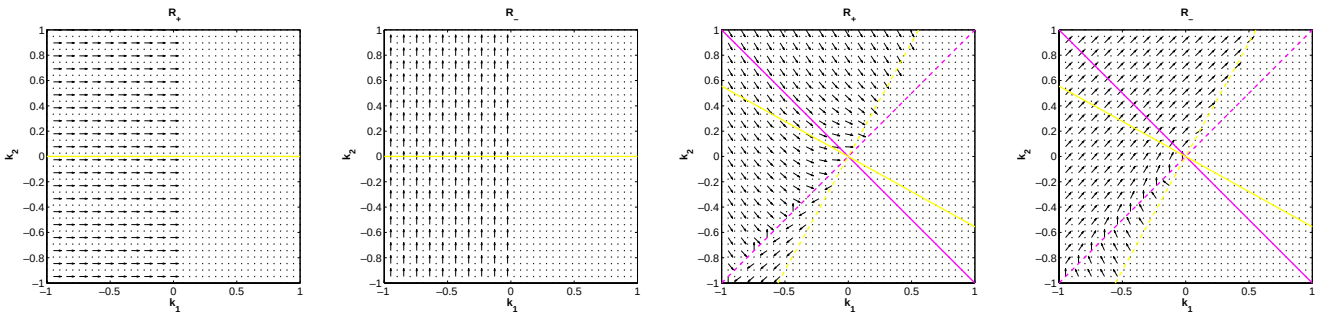

Fig. 14 Eigenvectors of the + and − modes. The *left two panels* are for the flat bottom case (associated with the upper row of Fig. 13), the *right two panels* are for a topographic case (third row of Fig. 13)

$\mathbf{R}_2 = (0, 1)^T$. These are the familiar flat bottom barotropic and first baroclinic modes (see first row of Fig. 13 and left two panels of Fig. 14).

Topographic case The solutions of Eq. 21 for the eigenfrequencies $\omega_i(\mathbf{K})$ with corresponding eigenvectors $\mathbf{R}_i(\mathbf{K})$ are real. One easily finds

$$\omega_\pm(\mathbf{K}) = \frac{1}{2}\left[\omega_A + \omega_L + \omega_R \pm \sqrt{(\omega_R - \omega_C)^2 + 4\omega_A(\omega_L + \omega_T - \omega_P)}\right]$$

$$\mathbf{R}_\pm(\mathbf{K}) = \begin{pmatrix} f\psi \\ E \end{pmatrix}_\pm = \frac{i}{\sqrt{\omega_T^2 + (\omega_\pm - \omega_R)^2}} \begin{pmatrix} \omega_T \\ \omega_R - \omega^\pm \end{pmatrix} \tag{23}$$

Approximately, $\omega_+ \approx \omega_R$ and $\omega_- \approx \omega_L + \omega_A(\omega_P - \omega_T)/\omega_R$. All specific frequencies $\omega_I, I = ACLPRT$, are asymmetric with respect to the wavevector, i.e., $\omega_I(\mathbf{K}) = -\omega_I(-\mathbf{K})$. We thus need the eigenfrequencies and eigenvectors only on a halfplane because $\omega_\pm(\mathbf{K}) = -\omega_\mp(-\mathbf{K})$ and correspondingly for the eigenvectors, $\mathbf{R}_\pm(\mathbf{K}) = (\mathbf{R}_\mp(-\mathbf{K}))^*$. It appears sensible to choose the halfplane $\mathbf{K} \cdot (\mathbf{k} \times \boldsymbol{\gamma}) > 0$ (i.e., positive component of the wavevector along the f/h contours, implying $k < 0$ for flat bottom). This choice is established in Fig. 13, which shows dispersion relations and group velocities for a few cases of gradients of topography. Figure 14 clearly demonstrates the mixed character of planetary–topographic wave modes: For non-zero topographic slopes, the modes are neither barotropic nor baroclinic but 'mixed'. A particular detailed discussion of this feature is found in Hallberg (1997) who used a two-layer quasigeostrophic model.

A few properties of these solutions are worth mentioning for use in the main body of the paper:

- Even for moderate slopes, the topographic β can be much larger than the planetary one, and the periods of topographic waves are much smaller than those of flat bottom waves. The maximum period of the baroclinic topographic mode (−wave) is about 100 days (see lower three rows of Fig. 13) compared to about 600 days for flat bottom.
- The +waves propagate most rapidly for wavevectors along $f/h = \text{const}$. For the −waves, this occurs for wavevectors across $f/h = \text{const}$. The speeds of topographic waves exceed those of flat bottom waves considerably (a factor of 10 is easily achieved). Speeds for +wave exceeds typically 10 m s^{-1}, and for the −wave, we find values as large as 0.1 m s^{-1} (note that the scale in Fig. 13 is logarithmic).

References

Aoki S (2002) Coherent sea level response to the antarctic oscillation. Geophys Res Lett 29(20):1950, 0094–8276

Borowski D, Gerdes R, Olbers D (2002) Thermohaline and wind forcing of a circumpolar channel with blocked geostrophic contours. J Phys Oceanogr 32:2520–2540

Charney JG, DeVore JG (1979) Multiple flow equilibra in the atmosphere and blocking. J Atmos Sci 36:1205–1216

Cunningham S, Pavic M (2007) Surface geostrophic currents across the Antarctic Circumpolar Current in drake passage from 1992 to 2004. Prog Oceanogr 73:296–310

Cunningham SA, Alderson SG, King BA, Brandon MA (2003) Transport and variability of the Antarctic Circumpolar Current in Drake Passage. J Geophys Res 108: nO. C5, 8084

Gent PR, Large WG, Bryan FO (2001) What sets the mean transport through Drake Passage? J Geophys Res 106: 2693–2712

Gille ST (1999) Evaluating southern ocean response to wind forcing. Physics And Chemistry Of The Earth Part A Solid Earth Geodesy, 24(4):423–428, 1464–1895

Hall A, Visbeck M (2002) Synchronous variability in the southern hemisphere atmosphere, sea ice, and ocean resulting from the annular mode. J Clim 15(21):3043–3057

Hallberg R (1997) Localized coupling between surface- and bottom-intensified flow over topography. J Phys Oceanogr 27:977–998

Hallberg R, Gnanadesikan A (2006) The role of eddies in determining the structure and response of the wind-driven southern hemisphere overturning: results from the Modeling Eddies in the Southern Ocean (MESO) project. J Phys Oceanogr 36:2232–2252

Hasselmann K (1976) Stochastic climate models, part I: theory. Tellus 28:473–485

Hughes CW, Meredith CP (2006) Coherent sea-level fluctuations along the global continental slope. Philos Trans R Soc Lond A 364(1841):885–901, Mathematical Physical And Engineering Sciences

Hughes CW, Meredith MP, Heywood K (1999) Wind driven transport fluctuations through Drake Passage: a southern mode. J Phys Oceanogr 29:1971–1992

Hughes CW, Woodworth PL, Meredith MP, Stepanov V, Whitworth T, Pyne AR (2003) Coherence of antarctic sea levels, southern hemisphere annular mode, and flow through Drake Passage. Geophys Res Lett 30(9): 0094-8276 1464

Lettmann K (2006) Untersuchungen zur Variabilität im Südlichen Ozean mit dem Ozeanzirkulationsmodel BARBI. PhD thesis, University Bremen

Meredith MP, Woodworth PL, Hughes CW, Stepanov V (2004) Changes in the ocean transport through Drake Passage during the 1980s and 1990s, forced by changes in the southern annular mode. Geophys Res Lett 31(21): 0094-8276 L21305

Meredith MP, Vassie JM, Heywood KJ, Spencer R (1996) On the temporal variability of the transport through drake passage. J Geophys Res 101:22485–22494

Olbers D, Eden C (2003) A simplified general circulation model for a baroclinic ocean with topography. part I: theory, waves and wind-driven circulations. J Phys Oceanogr 33:2719–2737

Olbers D, Völker C (1996) Steady states and variability in oceanic zonal flows. In: Anderson DLT, Willebrand J (eds) Decadal climate variability dynamics and predicition. Springer, Berlin, pp 407–443

Olbers D, Borowski D, Völker C, Wolff J-O (2004) The dynamical balance, transport and circulation of the antarctic circumpolar current. Antarct Sci 16(4):439–470

Olbers D, Lettmann K, Wolff J-O (2007) Wave-induced topographic formstress in baroclinic channel flow. Ocean Dyn doi:10.1007/s10236-007-0109-2

Olbers D, Lettmann K, Timmermann R (2006) Six circumpolar currents—on the forcing of the Antarctic Circumpolar Current by wind and mixing. Ocean Dyn 57:12–31. doi:10.1007/s10236-006-0087-9

Rhines P (1977) The dynamics of unsteady currents. In: Goldberg E (ed) The sea, vol VI. Wiley, New York, pp 189–318

Rintoul SR, Hughes C, Olbers D (2001) The Antarctic Circumpolar Current system. In: Siedler G, Church J, Gould J (eds) Ocean circulation and climate. Academic, New York, pp 271–302

Rintoul SR, Sokolov S, Church J (2002) A 6 year record of baroclinic transport variability of the Antarctic circumpolar current at 140 degrees E derived from expendable bathythermograph and altimeter measurements. J Geophys Res 107

Sura P, Gille ST (2003) Interpreting wind-driven southern ocean variability in a stochastic framework. J Mar Res 61(3):313–334, 0022-2402.

Tansley CE, Marshall DP (2001) On the dynamics of wind-driven circumpolar currents. J Phys Oceanogr 31:3258–3273

Thompson DWJ, Wallace JM (2000) Annular modes in the extratropical circulation. Part I: month-to-month variability. J Climate 13(5):1000–1016, 0894–8755

Vivier F, Kelly KA, Harismendy M (2005) Causes of large-scale sea level variations in the Southern Ocean: Analyses of sea level and a barotropic model. J Geophys Res-Oceans, 110(C9):C09014

Völker C (1999) Momentum balance in zonal flows and resonance of baroclinic Rossby waves. J Phys Oceanogr 29: 1666–1681

von Storch H, Zwiers FW (1999) Statistical analysis in climate research. Cambrige Univ. Press

Wearn Jr RB, Baker Jr DJ (1980) Bottom pressure measurements across the Antarctic circumpolar current and their relation to the wind. Deep-Sea Res 27A:875–888

Webb D, de Cuevas B, Coward A (1998) The first main run of the occam global model. Southampton Oceanography Centre, Internal Report SOC, UK (34)

Weijer W, Gille ST (2005) Adjustment of the southern ocean to wind forcing on synoptic time scales. J Phy Oceanogr 35(11):2076–2089, 0022–3670

Whitworth III T, Peterson RG (1985) Volume transport of the Antacrtic circumpolar current from bottom pressure measurements. J Phys Oceanogr 15:810–816

Willebrand J, Philander SGH, Pacanowski RC (1980) The oceanic response to large-scale atmospheric disturbances. J Phys Oceanogr 10(3):411–429